APL Materials

Strain-engineering of charge transport in the correlated Dirac semimetal of perovskite $CaIrO_3$ thin films

Cite as: APL Mater. **7**, 081115 (2019); https://doi.org/10.1063/1.5109582
Submitted: 09 May 2019 . Accepted: 22 July 2019 . Published Online: 16 August 2019

M. Masuko, J. Fujioka, M. Nakamura, M. Kawasaki, and Y. Tokura

Strain-engineering of charge transport in the correlated Dirac semimetal of perovskite $CaIrO_3$ thin films

Cite as: APL Mater. 7, 081115 (2019); doi: 10.1063/1.5109582
Submitted: 9 May 2019 • Accepted: 22 July 2019 •
Published Online: 16 August 2019

M. Masuko,[1,a] J. Fujioka,[2,3,b] M. Nakamura,[3,4] M. Kawasaki,[1,4] and Y. Tokura[1,4,5]

AFFILIATIONS

[1] Department of Applied Physics and Quantum Phase Electronics Center (QPEC), University of Tokyo, Bunkyo-ku, Tokyo 113-8656, Japan
[2] Graduate School of Pure and Applied Sciences, University of Tsukuba, 1-1-1 Tennodai, Tsukuba, Ibaraki 305-8573, Japan
[3] PRESTO, Japan Science and Technology Agency, Kawaguchi 332-0012, Japan
[4] RIKEN Center for Emergent Matter Science (CEMS), Wako, Saitama 351-0198, Japan
[5] Tokyo College, University of Tokyo, Bunkyo-ku, Tokyo 113-8656, Japan

[a] Electronic mail: masuko@cmr.t.u-tokyo.ac.jp
[b] Electronic mail: fujioka@ims.tsukuba.ac.jp

ABSTRACT

We have investigated the charge transport in thin films of correlated Dirac semimetal of perovskite $CaIrO_3$ by measurements of resistivity and optical spectra. The semimetallic transport of either electron-type or hole-type carrier is observed in the strain-relaxed thin films. By controlling the strain relaxation via thermal annealing, the carrier density decreases in both *n*-type and *p*-type samples, while enhancing the carrier mobility up to 160 $cm^2\ V^{-1}\ s^{-1}$ at an electron density of $2.5 \times 10^{18}\ cm^{-3}$ at 2 K. We propose that the energy of Dirac line node, which locates in proximity to the Fermi level, varies with the lattice distortion or strain-sensitive defect character, causing the sign change in the charge carrier as well as the mobility enhancement.

The interplay between the electron correlation and spin-orbit coupling in heavy transition-metal oxides offers a fertile ground to develop emergent topological phases with potential for electronic device application. A remarkable example is the Dirac/Weyl semimetal, wherein the highly mobile electron with massless or small effective-mass character can give rise to unusual charge transport such as the giant magnetoresistivity (MR) or the anomalous Hall effect.[1–6] The perovskite $AIrO_3$ (A = Sr, Ca) is one such candidate, which hosts the correlated Dirac semimetal on the verge of Mott transition.[7–10] In $AIrO_3$, the nominally tetravalent Ir-ion has five electrons in the $5d\ t_{2g}$ orbitals, which split into fully occupied $j_{\mathrm{eff}} = 3/2$ states and half-filled $j_{\mathrm{eff}} = 1/2$ state by the relativistic spin-orbit interaction. The electronic states around the Fermi energy are dominated by the half-filled $j_{\mathrm{eff}} = 1/2$ state with the strong electron correlation and thus provide an ideal playground for the Mott physics of Dirac electron. The theoretical studies propose that the Dirac line node is protected by the nonsymmorphic symmetry inherent to the orthorhombic perovskite structure (space group *Pbnm*) and thus is robust against the perturbation which keeps the symmetry intact.[7,9–13] In a thin film of $SrIrO_3$, the Dirac node is observed by the angle-resolved photoemission spectroscopy to position about 50 meV below the Fermi energy and generates small electron pocket(s).[10] More recently, it has been demonstrated that for the single crystalline bulk of $CaIrO_3$, the Dirac line node is remarkably close to the Fermi energy E_F and gives rise to highly mobile electrons with the mobility exceeding 60 000 $cm^2\ V^{-1}\ s^{-1}$ in the strongly correlated regime near the Mott transition.[14] Therein, the quantum limit of the Landau level is reached at a modest magnetic field of about 9 T, which has led to the giant positive magnetoresistivity (MR) with the MR ratio of 5000% due perhaps to the quasi-one-dimensional confinement of correlated Dirac electrons.

To exploit such quantum transport of Dirac electron to emergent functions of electronic devices, as the first step, it is necessary to realize the highly mobile Dirac electron in a thin film form. The epitaxial strain may be one of the promising ways to control the energy dispersion or topology of Dirac band via the modulation of the effective one-electron bandwidth or electron correlation. So far, the charge transport has been extensively studied for the epitaxially strained films of $SrIrO_3$,[15–23] yet a salient feature of highly mobile Dirac electron has not been identified. It has been pointed out that the Dirac line node is sensitive to the crystal symmetry and thus can be easily gapped out by the lattice distortion which is caused by the epitaxial strain and breaks the orthorhombic crystal symmetry.[18,24–26] In this context, the strain-free thin films of $CaIrO_3$, which keeps the orthorhombic crystal structure as in the bulk, is required to observe the charge transport of Dirac electrons in thin films but has remained elusive.[27–29]

In this paper, we demonstrate that the carrier density and mobility can be significantly controlled by the epitaxial strain combined with thermal annealing procedure in the thin films of $CaIrO_3$. In particular, the charge carrier is of electron-type and the mobility is enhanced up to 160 $cm^2\ V^{-1}\ s^{-1}$ at 2 K when the electron density is reduced down to 2.5×10^{18} cm^{-3} in the strain-relaxed films obtained by annealing the compressively strained films. On the contrary, the hole-type carriers govern the charge transport in the strain-relaxed films obtained by annealing the tensilely strained films. We anticipate that the charge transport is governed by the Dirac electrons at low temperatures, wherein the energy variation of the Dirac line node by the strain causes the sign change in the carrier-type as well as the mobility variation.

Thin film samples were fabricated by means of the pulsed laser deposition (PLD) technique using a KrF excimer laser (λ = 248 nm) on various substrates of $LaAlO_3$ (LAO) (110), LAO(001), $(LaAlO_3)_{0.3}(SrAl_{0.5}Ta_{0.5}O_3)_{0.7}$ (LSAT) (001), and $SrTiO_3$ (STO) (001). Hereafter, we denote the crystal orientations and reflection indices of substrate in the pseudocubic notation, unless otherwise noted as a_o, b_o, and c_o for orthorhombic (*Pbnm*) notation of $CaIrO_3$.[30] Although $CaIrO_3$ could not be directly grown on LAO(110), we found that the insertion of the buffer layer of the perovskite $CaTiO_3$ enables the growth of $CaIrO_3$ on LAO(110), as illustrated in Fig. 1(a). In the case of LAO(001), the perovskite $SrTiO_3$ was inserted as a buffer layer. The thickness of $CaTiO_3$ ($SrTiO_3$) was 1 nm (3 nm), and we confirmed that the buffer layers can be coherently grown on substrates. For simplicity, we hereafter express these samples as $CaIrO_3$/LAO(110) and $CaIrO_3$/LAO(001), respectively. The thickness of $CaIrO_3$ was about 80 nm or 30 nm for the films on LAO(110) and 30 nm for other substrates (see Table S1 of the supplementary material for the thicknesses of all samples). For the growth of $CaIrO_3$, we optimized the growth condition to the growth temperature at 590 °C and the oxygen pressure (P_{O_2}) at 50 mTorr, and the repetition and energy density of laser pulses were 2 Hz and 1.2 J cm^{-2}, respectively. Because of the volatility of Ir-ion,[18,31,32] the amorphous film of $CaTiO_3$ with a thickness 30 nm was deposited as a capping layer on the respective films at room temperature and P_{O_2} = 0.1 mTorr in order to protect $CaIrO_3$ from volatilization during the thermal annealing procedure. After the deposition, we divided the sample into some pieces. One of them was measured as the as-grown film, while others were annealed in ambient atmosphere at various temperatures in the range of 900–1400 °C for typically 1 h (see Table S1 and Fig. S4 of the supplementary material for the annealing conditions and transport properties of all samples). The resistivity and Hall resistivity were measured by means of the four-probe method. The reflectivity spectra were measured for the film without the capping layer by using a Fourier transform spectrometer (0.005–0.7 eV) and a grating-type monochromator equipped with a microscope (0.5–5 eV). The reflectivity spectra in the energy region of 4–30 eV were measured at room temperature with the use of synchrotron radiation at UV-SOR, Institute for Molecular Science, Japan. The optical conductivity spectra were obtained by the Kramers-Kronig analysis with the use of a two-layer model consisting of the film and substrate.

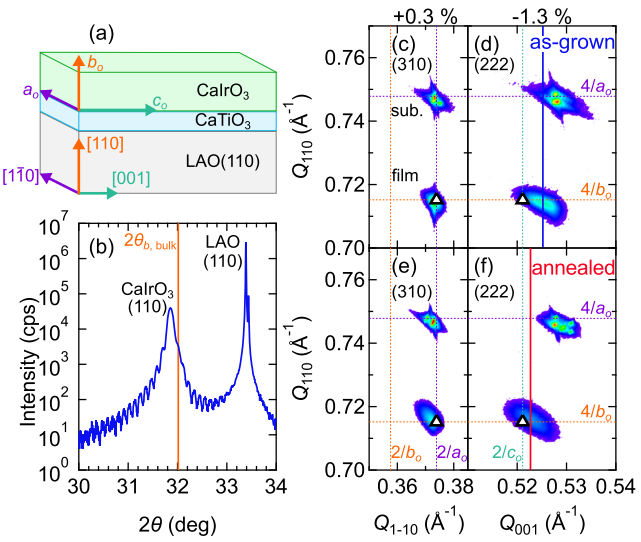

FIG. 1. (a) Schematic of single crystalline epitaxial $CaIrO_3$ grown on LAO(110) with the buffer layer of $CaTiO_3$. (b) X-ray diffraction 2θ-ω scan around (110) reflection for the as-grown $CaIrO_3$/LAO(110). Orange line represents the expected angle $2\theta_{b,bulk}$ of $[010]_o$ reflection of the bulk sample, which corresponds to the strain-free films oriented as illustrated in (a). The thickness of $CaIrO_3$ is 83 nm. [(c) and (d)] Reciprocal space mappings for as-grown $CaIrO_3$/LAO(110) around (310) and (222) reflection and (e, f) those for the annealed $CaIrO_3$/LAO(110). In (c)–(f), dashed lines represent the reciprocal lattice constants of the bulk $CaIrO_3$, and the lattice mismatch with the substrate is given on the top. White triangle symbols represent the expected peak positions of the film if $CaIrO_3$ is oriented as illustrated in (a) and its lattice constants are the same as bulk ones. Blue (red) line in (d) [(f)] represents the horizontal peak position of the as-grown (annealed) film. The indices, e.g., [110] and (110), are in the pseudocubic notation of perovskite, while a_o, b_o, and c_o are in the orthorhombic notation.

First, we investigated the films grown on the LAO(110) substrate to minimize the epitaxial strain. The lattice mismatch between $CaIrO_3$ and LAO (=3.789 Å) is relatively small for the a_o- and c_o-axes: +0.3% along the a_o-axis ($a_o/\sqrt{2}$ = 3.782 Å) and −1.3% along the c_o-axis ($c_o/2$ = 3.838 Å). In contrast, for the b_o-axis, the lattice mismatch is −4.3%, which is much larger than the other two. Here, the sign of lattice mismatch is positive (negative) when the lattice constant of the film is smaller (larger) than that of the substrate, which corresponds to the tensile (compressive) epitaxial strain. Hence, it is expected that $CaIrO_3$ is coherently grown on the

(110)-surface of LAO with the a_o-axis and c_o-axis oriented along the [1$\bar{1}$0] and [001]-direction (in-plane), respectively, and the b_o-axis oriented along [110] (out-of-plane), as illustrated in Fig. 1(a). This is confirmed by the X-ray diffraction (XRD) patterns for the as-grown film, as shown in Figs. 1(b)–1(d). The (110)-reflection (denoted in the pseudocubic notation) of $CaIrO_3$ is clearly observed around 31.8° with clear Laue fringes, while the peak angle is smaller than that expected from the lattice constant of the b_o-axis of the bulk. The reciprocal space mappings (RSMs) around (310)- and (222)-reflections are shown in Figs. 1(c) and 1(d), respectively. The positions of both reflections are roughly coincident with those expected from the bulk samples (represented by triangle markers), but the (222)-reflection of the film slightly shifts toward larger (001)-direction than that of the bulk. These results indicate that the lattice constant of the a_o-axis of the film is nearly identical to that of the bulk, while that of b_o- (c_o-) axis is slightly larger (smaller) for the film due to the compressive-strain along the [001]-direction (in-plane). It is noted that the position of the (222)-reflections of the film is different from that of the substrate along the [001]-direction, which indicates the partial relaxation of the film due to the large film thickness (83 nm). In the thermally annealed films, as shown in Fig. 1(f), the (222)-reflection of the film nearly coincides with that of the bulk, suggesting that the compressive strain is significantly reduced. Note that the elongation of lattice constants, which is possibly caused by the off-stoichiometry,[31,32] is not found in XRD for all annealed samples, suggesting that the capping layer works. The similar lattice relaxation is observed for the annealed $CaIrO_3$/LAO(001), as shown in Figs. S2(a) and S2(b) of the supplementary material. On the contrary, the strong and weak tensile strain appears to be imposed for the films on STO(001) (+1.2%) and LSAT(001) (+0.3%) substrates, respectively (Figs. S1–S3). As shown in Figs. S2(e) and S2(f) of the supplementary material, for STO(001), the in-plane (out-of-plane) lattice constant of the as-grown thin film is larger (smaller) than that of the bulk,[27] while the thermal annealing significantly relaxes the tensile strain as well. Thus, the epitaxial strain is significantly relaxed by the thermal annealing in both the compressively strained and tensilely strained cases. Incidentally, for LSAT(001), the lattice mismatch between the substrate and the film is so small that the precise evaluation of lattice constants of the film from the XRD patterns is difficult [Figs. S1, S2(c), and S2(d)].

We first discuss the transport property of $CaIrO_3$ grown on LAO(110) and LAO(001), in which compressive-strain is applied in the as-grown case. Note that all these samples exhibit electron-type charge transport in both the as-grown and annealed films as is the case of bulk samples.[14] In Fig. 2(a), we show the temperature dependence of resistivity for the as-grown $CaIrO_3$/LAO(110) (blue). The resistivity shows semimetallic temperature dependence and moderately increases as temperature decreases in accordance with the previous reports.[27,28] Figure 2(c) shows the Hall resistivity (ρ_{yx}) of the as-grown $CaIrO_3$/LAO(110). ρ_{yx} shows a moderate temperature variation but remains to be nearly linear as a function of magnetic field B at all temperatures. Here, we define the Hall coefficient R_H as the slope of ρ_{yx} at $B = 0$. The sign of R_H remains to be negative at all temperatures, indicating that the charge transport is governed by electron-type carriers. We plot the temperature dependence of $1/e|R_H|$ as a measure of the carrier density in Fig. 2(b), which monotonically decreases as temperature decreases. For comparison, the resistivity and $1/e|R_H|$ for the single crystalline bulk

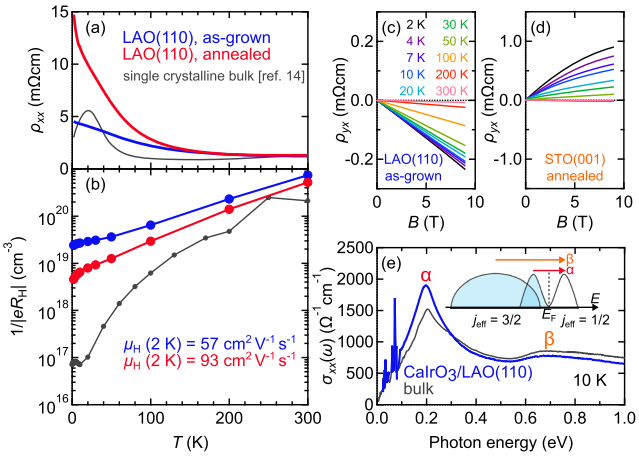

FIG. 2. (a) Resistivity and (b) carrier density of $CaIrO_3$/LAO(110) thin films as a function of temperature for as-grown (blue) and annealed (red) samples. The data of single crystalline bulk $CaIrO_3$ (gray) (from Ref. 14) are also shown for comparison. The values in (b) are the carrier mobility of the plotted samples at 2 K. [(c) and (d)] Magnetic field dependence of Hall resistivity for the as-grown $CaIrO_3$/LAO(110) and annealed $CaIrO_3$/STO(001). The annealing condition was 1100 °C and 1 h for both LAO(110) and STO(001). (e) Optical conductivity spectra for the as-grown $CaIrO_3$/LAO(110) (blue) and bulk sample (gray) at 10 K. The inset schematically illustrates the density of states and respective (α and β) optical transitions in $CaIrO_3$.

sample (gray, reproduced from Ref. 14) are also plotted in Figs. 2(a) and 2(b), respectively. The behaviors of the resistivity and $1/e|R_H|$ for the film are qualitatively consistent with the results of the bulk except a downturn of resistivity below 20 K.[14] In the bulk sample, it is demonstrated that the thermally excited carriers at the Dirac band are responsible for the temperature dependence of resistivity and Hall resistivity; the apparent carrier density decreases and thus the resistivity increases with lowering temperatures, whereas the reduction in carrier density is compensated by the mobility enhancement at low temperature, resulting in the resistivity-downturn.[14] The similarity in the temperature dependence of resistivity and Hall resistivity between the film and the bulk except the resistivity-downturn indicates that the charge transport in the thin film is also governed by the Dirac electrons. In the scheme of single carrier model, which is valid in the bulk sample, the typical carrier density ($n_H = 1/e|R_H|$) and the mobility ($\mu_H = 1/\rho_{xx}|R_H|$) are about 2.4×10^{19} cm^{-3} and 57 cm^2 V^{-1} s^{-1}, respectively, at 2 K for the as-grown $CaIrO_3$/LAO(110).

We also show the resistivity and $1/e|R_H|$ for the annealed $CaIrO_3$/LAO(110) (red) in Figs. 2(a) and 2(b), respectively. The overall behaviors are consistent with those of the as-grown one except the following aspects; compared to those for the as-grown one, the resistivity increases more steeply below 100 K, and $1/e|R_H|$ become smaller especially at low temperatures. In the annealed $CaIrO_3$/LAO(110), $n_H = 4.6 \times 10^{18}$ cm^{-3} and $\mu_H = 93$ cm^2 V^{-1} s^{-1} at 2 K, which are lower and higher than those of the as-grown one, respectively. A similar behavior is also observed in the as-grown and annealed $CaIrO_3$/LAO(001). To be noted for the annealed $CaIrO_3$/LAO(001) are that n_H is reduced down to 2.5×10^{18} cm^{-3} and that μ_H is significantly enhanced up to 160 cm^2 V^{-1} s^{-1} at 2 K.

To clarify the electronic structure in the thin film, we have explored the charge dynamics by means of the optical conductivity spectra $\sigma_{xx}(\omega)$. As shown in Fig. 2(e), $\sigma_{xx}(\omega)$ of the as-grown $CaIrO_3$/LAO(110) shows two peaks around 0.2 eV (α-peak) and 0.7 eV (β-peak), respectively. The spectral shape and peak energy are consistent with those of the bulk $CaIrO_3$. As is the case of $SrIrO_3$[33] and Sr_2IrO_4,[34] these peaks are assigned to the optical transition between the occupied j_{eff} = 1/2- and unoccupied j_{eff} = 1/2-states and that between the occupied j_{eff} = 3/2- and unoccupied j_{eff} = 1/2- states, respectively, as illustrated in the inset of Fig. 2(e). The coincidence of peak energy and spectral shape between the bulk and the thin film suggests that the electronic structure of the thin film is similar to that of the bulk sample.

On the other hand, the behavior of R_H is more complicated for the films grown on STO(001) and LSAT(001), in which tensile-strain is applied in the as-grown samples. For the as-grown $CaIrO_3$/STO(001) and $CaIrO_3$/LSAT(001), the sign of R_H at low temperatures varies from sample to sample. However, for the annealed $CaIrO_3$/STO(001), the all samples exhibit positive R_H at low temperatures, which differs from the negative-R_H behavior for the films on LAO(110) and LAO(001) and the bulk sample.[14] For the annealed $CaIrO_3$/LSAT(001), the sign of R_H at low temperatures depends on the annealing temperature; $R_H > 0$ in the samples annealed at $\lesssim$1200 °C, whereas $R_H < 0$ in the ones annealed at $\gtrsim$1200 °C. To discuss the charge transport of hole-type carriers, we focus on the annealed $CaIrO_3$/STO(001), but the main features are similar for the annealed $CaIrO_3$/LSAT(001) with positive R_H. Figure 2(d) exemplifies ρ_{yx} for the annealed $CaIrO_3$/STO(001). ρ_{yx} is slightly nonlinear as a function of magnetic field at low temperatures. R_H shows a thermally induced sign change, which is often seen in semiconductors or semimetals with the bipolar carrier transport. Interestingly, the sign of R_H is positive below 50 K, suggesting that the charge transport is governed by hole-type carriers at low temperatures. Moreover, μ_H of the annealed $CaIrO_3$/STO(001) reaches as high as 83 $cm^2\ V^{-1}\ s^{-1}$ with the typical hole density $p_H = 4.4 \times 10^{18}\ cm^{-3}$. In Figs. 3(b) and 3(c), the mobility of p-type and n-type samples is plotted as a function of carrier density, respectively. We note that the mobility increases up to the optimum annealing temperature T^* and then decreases above T^* as a function of annealing temperature, as shown in Fig. S4. Here, we plot the results below T^*, wherein the lattice imperfection during the annealing is expected to be minimal, in Figs. 3(b) and 3(c). It is evident that, in both p-type and n-type samples, the mobility is enhanced as the carrier density decreases. The results also show that the annealed samples tend to exhibit higher mobility and lower carrier density than those in as-grown samples. We note that the relatively high mobility hole with the low carrier density has been reported for neither bulk nor thin film samples of $AIrO_3$ so far.

These results demonstrate that the charge transport is governed by the electron-type carriers for the compressively strained films grown on LAO(110) and LAO(001) and their annealed films but is governed by the hole-type carriers for the annealed films grown on STO(001) and LSAT(001). Here, we discuss the possible origin of the observed hole-type carriers. According to the theoretical calculations,[9,14,35] in addition to the Dirac line node, the normal band crosses the Fermi energy nearby the Γ-point in the momentum space and yields a hole pocket with the effective mass more than 1.0 m_0

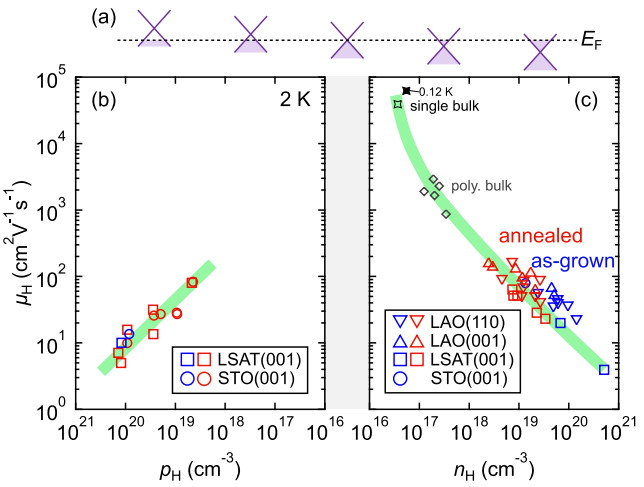

FIG. 3. (a) Schematics of the energy change in the Dirac node. [(b) and (c)] Mobility as a function of carrier density at 2 K for p-type and n-type $CaIrO_3$ thin films grown on four kinds of substrates. Blue (red) symbols represent the data for the as-grown (annealed) samples. The data for single crystalline bulk $CaIrO_3$ (2 K and 0.12 K) from Ref. 14 and those for polycrystalline bulk ones (2 K), which are prepared in the similar condition in Ref. 14, are also plotted for comparison. Green lines are guides to the eyes.

(m_0 is the free electron mass). However, it is not likely that the mobility of massive hole is enhanced up to 83 $cm^2\ V^{-1}\ s^{-1}$ at the carrier density of as low as $4.4 \times 10^{18}\ cm^{-3}$ in the correlated electron oxide. A more plausible scenario is that the energy of the Dirac line node varies with the strain and annealing condition. Specifically, the Dirac line node is located perhaps below the Fermi energy in the compressively strained films and their annealed ones as confirmed for the case of bulk.[14] On the contrary, it may be slightly above the Fermi energy in the annealed ones which have been tensilely strained in the as-grown state, yielding the hole-type carrier with relatively high mobility, as illustrated in Fig. 3(a). A possible reason why the initial epitaxial strain in the as-grown state significantly affects the carrier type or the energy of the Dirac line node even in the strain-relaxed films is the change in the band structure due to lattice distortion. Indeed, the energy and shape of the Dirac line node are predicted to be sensitive to the electron hopping or effective electron correlation.[7,14] Another possibility is the density or character of the defect, which depends on the epitaxial strain in the as-grown state, may cause such strain-sensitive charge transport in this correlated Dirac semimetal. The slight change in the density of O^{2-}- or Ir^{4+}-vacancies, which could not be quantified by the XRD, can modify the band structure around the Fermi energy or effective electron correlation. The fact that $CaIrO_3$/LAO(110) with the significant Ir^{4+}-vacancy, in which the Fermi energy would be lowered, remains to be of n-type suggests that the sign-change in carrier type cannot be straightforwardly explained by the rigid band-shift. Toward the fine tuning of the Dirac node to the Fermi energy in thin films of $CaIrO_3$, our results suggest that one must carefully consider the epitaxial strain and lattice imperfection, which would sensitively change the energy of Dirac node even in the strain-relaxed films.

In conclusion, we show that the carrier density and mobility significantly change by controlling the epitaxial strain and its relaxation via the thermal annealing procedure for thin films of correlated Dirac semimetal of perovskite $CaIrO_3$. The results of magnetotransport measurements show that the charge transport is governed by electron-type carriers for the compressively strained films and their annealed ones but is dominated by hole-type carriers for strain-relaxed films which have been tensilely strained in the as-grown state. By controlling the lattice-relaxation, the mobility of the electron- or hole-type carrier is typically enhanced up to 160 $cm^2\ V^{-1}\ s^{-1}$ at 2 K as the carrier density decreases. We anticipate that the energy change in the Dirac line node coupled to the lattice distortion or defects causes such a variation of electron/hole-type charge transport in this correlated Dirac semimetal.

See supplementary material for XRD $2\theta - \omega$ scans for the as-grown $CaIrO_3$ films grown on (001)-oriented substrates [LAO(001), LSAT(001), and STO(001)] (Fig. S1), RSM for the as-grown and annealed films on (001)-oriented substrates (Fig. S2), in-plane and out-of-plane lattice constants of the films on (001)-oriented substrates as a function of the lattice constant of substrates (Fig. S3), carrier density and mobility at 2 K as a function of annealing temperature (Fig. S4), and film thickness, annealing conditions, and transport properties for all samples (Table S1).

We thank A. Tsukazaki, R. Yamada, K. S. Takahashi, J. Matsuno, S. Sakai, M. Hirayama, and R. Arita for useful discussions. This work was partly supported by the Grant-In-Aid for Science Research (Grant Nos. 16H00981, 18H01171, 18H04214, and 16H06345) from the MEXT and by PRESTO (Grant No. JPMJPR15R5) and CREST (Grant No. JPMJCR16F1), JST, Japan.

REFERENCES

[1] N. P. Armitage, E. J. Male, and A. Vishwanath, Rev. Mod. Phys. **90**, 015001 (2018).
[2] T. Liang, Q. Gibson, M. N. Ali, M. Liu, R. J. Cava, and N. P. Ong, Nat. Mater. **14**, 280 (2014).
[3] J. Xiong, S. K. Kushwaha, T. Liang, J. W. Krizan, M. Hirschberger, W. Wang, R. J. Cava, and N. P. Ong, Science **350**, 413 (2015).
[4] Z. Fang, N. Nagaosa, K. S. Takahashi, A. Asamitsu, R. Mathieu, T. Ogasawara, H. Yamada, M. Kawasaki, Y. Tokura, and K. Terakura, Science **302**, 92 (2003).
[5] R. Mathieu, A. Asamitsu, H. Yamada, K. S. Takahashi, M. Kawasaki, Z. Fang, N. Nagaosa, and Y. Tokura, Phys. Rev. Lett. **93**, 016602 (2004).
[6] T. Suzuki, R. Chisnell, A. Devarakonda, Y.-T. Liu, W. Feng, D. Xiao, J. W. Lynn, and J. G. Checkelsky, Nat. Phys. **12**, 1119 (2016).
[7] J.-M. Carter, V. V. Shankar, M. A. Zeb, and H.-Y. Kee, Phys. Rev. B **85**, 115105 (2012).
[8] M. A. Zeb and H.-Y. Kee, Phys. Rev. B **86**, 085149 (2012).
[9] H. Zhang, K. Haule, and D. Vanderbilt, Phys. Rev. Lett. **111**, 246402 (2013).
[10] Y. F. Nie, P. D. C. King, C. H. Kim, M. Uchida, H. I. Wei, B. D. Faeth, J. P. Ruf, J. P. C. Ruff, L. Xie, X. Pan, C. J. Fennie, D. G. Schlom, and K. M. Shen, Phys. Rev. Lett. **114**, 016401 (2015).
[11] C. Fang, Y. Chen, H.-Y. Kee, and L. Fu, Phys. Rev. B **92**, 081201(R) (2015).
[12] Y. Chen, Y.-M. Lu, and H.-Y. Kee, Nat. Commun. **6**, 6593 (2015).
[13] Y. Chen, H.-S. Kim, and H.-Y. Kee, Phys. Rev. B **93**, 155140 (2016).
[14] J. Fujioka, R. Yamada, M. Kawamura, S. Sakai, M. Hirayama, R. Arita, T. Okawa, D. Hashizume, M. Hoshino, and Y. Tokura, Nat. Commun. **10**, 362 (2019).
[15] Y. Liu, H. Masumoto, and T. Goto, Mater. Trans. **46**, 100 (2005).
[16] S. Y. Jang, H. Kim, S. J. Moon, W. S. Choi, B. C. Jeon, J. Yu, and T. W. Noh, J. Phys.: Condens. Matter **22**, 485602 (2010).
[17] A. Biswas, K.-S. Kim, and Y. H. Jeong, J. Appl. Phys. **116**, 213704 (2014).
[18] K. R. Kleindienst, K. Wolff, J. Schubert, R. Schneider, and D. Fuchs, Phys. Rev. B **98**, 115113 (2018).
[19] N. Manca, D. J. Groenendijk, I. Pallecchi, C. Autieri, L. M. K. Tang, F. Telesio, G. Mattoni, A. McCollam, S. Picozzi, and A. D. Caviglia, Phys. Rev. B **97**, 081105(R) (2018).
[20] A. Gutiérrez-Llorente, L. Iglesias, B. Rodríguez-González, and F. Rivadulla, APL Mater. **6**, 091101 (2018).
[21] C. C. Fan, Z. T. Liu, S. H. Cai, Z. Wang, P. Xiang, K. L. Zhang, W. L. Liu, J. S. Liu, P. Wang, Y. Zheng, D. W. Shen, and L. X. You, AIP Adv. **7**, 085307 (2017).
[22] D. J. Groenendijk, C. Autieri, J. Girovsky, M. C. Martinez-Velarte, N. Manca, G. Mattoni, A. M. R. V. L. Monteiro, N. Gauquelin, J. Verbeeck, A. F. Otte, M. Gabay, S. Picozzi, and A. D. Caviglia, Phys. Rev. Lett. **119**, 256403 (2017).
[23] L. Hao, D. Meyers, C. Frederick, G. Fabbris, J. Yang, N. Traynor, L. Horak, D. Kriegner, Y. Choi, J.-W. Kim, D. Haskel, P. J. Ryan, M. P. M. Dean, and J. Liu, Phys. Rev. Lett. **119**, 027204 (2017).
[24] J. Liu, D. Kriegner, L. Horak, D. Puggioni, C. R. Serrao, R. Chen, D. Yi, C. Frontera, V. Holy, A. Vishwanath, J. M. Rondinelli, X. Marti, and R. Ramesh, Phys. Rev. B **93**, 085118 (2016).
[25] Z. T. Liu, M. Y. Li, Q. F. Li, J. S. Liu, W. Li, H. F. Yang, Q. Yao, C. C. Fan, X. G. Wan, Z. Wang, and D. W. Shen, Sci. Rep. **6**, 30309 (2016).
[26] L. Horák, D. Kriegner, J. Liu, C. Frontera, X. Marti, and V. Holý, J. Appl. Crystallogr. **50**, 385 (2017).
[27] D. Hirai, J. Matsuno, D. Nishio-Hamane, and H. Takagi, Appl. Phys. Lett. **107**, 012104 (2015).
[28] A. Biswas and Y. H. Jeong, J. Appl. Phys. **117**, 195305 (2015).
[29] Z. Guo, D. Lan, F. Jin, L. Qu, K. Zhuang, B. Chen, G. Gao, F. Chen, and W. Wu, J. Appl. Phys. **124**, 125308 (2018).
[30] Here, the [100]-, [010]- and [001]-direction in the orthorhombic notation corresponds to [1$\bar{1}$0]-, [110]- and [001]-direction in the pseudocubic notation.
[31] K. Nishio, H. Y. Hwang, and Y. Hikita, APL Mater. **4**, 036102 (2016).
[32] W. C. Yang, Y. T. Xie, W. K. Zhu, K. Park, A. P. Chen, Y. Losovyj, Z. Li, H. M. Liu, M. Starr, J. A. Acosta, C. G. Tao, N. Li, Q. X. Jia, J. J. Heremans, and S. X. Zhang, Sci. Rep. **7**, 7740 (2017).
[33] J. Fujioka, T. Okawa, A. Yamamoto, and Y. Tokura, Phys. Rev. B **95**, 121102(R) (2017).
[34] B. J. Kim, H. Jin, S. J. Moon, J.-Y. Kim, B.-G. Park, C. S. Leem, J. Yu, T. W. Noh, C. Kim, S.-J. Oh, J.-H. Park, V. Durairaj, G. Cao, and E. Rotenberg, Phys. Rev. Lett. **101**, 076402 (2008).
[35] H.-S. Kim, Y. Chen, and H.-Y. Kee, Phys. Rev. B **91**, 235103 (2015).